

ENRICO NICHELATTI

Dipartimento Fusione e Tecnologie per la Sicurezza Nucleare
Divisione Tecnologie Fisiche per la Sicurezza e la Salute
Laboratorio Micro e Nanostrutture per la Fotonica
Centro Ricerche Casaccia, Roma

F. BONFIGLI, M.A. VINCENTI, R.M. MONTEREALI

Dipartimento Fusione e Tecnologie per la Sicurezza Nucleare
Divisione Tecnologie Fisiche per la Sicurezza e la Salute
Laboratorio Micro e Nanostrutture per la Fotonica
Centro Ricerche Frascati, Roma

FABRIZIA SOMMA

Dipartimento di Scienze
Università Roma Tre, Roma

ANGELICA CECILIA, TILO BAUMBACH

Synchrotron Radiation Facility ANKA
Karlsruhe Institute of Technology (KIT), Germany

SYNCHROTRON X-RAY QUASI-FAR-FIELD IMAGING ON LUMINESCENT LITHIUM FLUORIDE DETECTORS

RT/2016/8/ENEA



ITALIAN NATIONAL AGENCY FOR NEW TECHNOLOGIES,
ENERGY AND SUSTAINABLE ECONOMIC DEVELOPMENT

ENRICO NICHELATTI

Dipartimento Fusione e Tecnologie per la Sicurezza Nucleare
Divisione Tecnologie Fisiche per la Sicurezza e la Salute
Laboratorio Micro e Nanostrutture per la Fotonica
Centro Ricerche Casaccia, Roma

F. BONFIGLI, M.A. VINCENTI, R.M. MONTEREALI

Dipartimento Fusione e Tecnologie per la Sicurezza Nucleare
Divisione Tecnologie Fisiche per la Sicurezza e la Salute
Laboratorio Micro e Nanostrutture per la Fotonica
Centro Ricerche Frascati, Roma

FABRIZIA SOMMA

Dipartimento di Scienze
Università Roma Tre, Roma

ANGELICA CECILIA, TILO BAUMBACH

Synchrotron Radiation Facility ANKA
Karlsruhe Institute of Technology (KIT), Germany

SYNCHROTRON X-RAY QUASI-FAR-FIELD IMAGING ON LUMINESCENT LITHIUM FLUORIDE DETECTORS

RT/2016/8/ENEA



ITALIAN NATIONAL AGENCY FOR NEW TECHNOLOGIES,
ENERGY AND SUSTAINABLE ECONOMIC DEVELOPMENT

I rapporti tecnici sono scaricabili in formato pdf dal sito web ENEA alla pagina
<http://www.enea.it/it/produzione-scientifica/rapporti-tecnici>

I contenuti tecnico-scientifici dei rapporti tecnici dell'ENEA rispecchiano
l'opinione degli autori e non necessariamente quella dell'Agenzia

The technical and scientific contents of these reports express the opinion
of the authors but not necessarily the opinion of ENEA.

SYNCHROTRON X-RAY QUASI-FAR-FIELD IMAGING ON LUMINESCENT LITHIUM FLUORIDE DETECTORS

Enrico Nichelatti, F. Bonfigli, M.A. Vincenti, R.M. Montereali, F. Somma, A. Cecilia, T. Baumbach

Abstract

Radiation imaging detectors based on luminescent colour centres (CC's) in lithium fluoride (LiF) have been recently demonstrated to be reliable, efficient, and with high spatial resolution across a large area. In this technical report, LiF crystals and films are tested as detectors for poly-energetic X-ray quasi-far-field imaging. The intensity and phase details of a test pattern are stored as a spatial distribution of CC's in a LiF detector plate; this information can be later recovered by exciting the plate with blue light and recording the obtained photoluminescence (PL) image at an optical microscope. A theoretical model is put forward for the interaction between X-rays and test pattern, and for the formation of CC's in LiF under X-irradiation. Details of calculated PL intensity maps are finally compared with experimentally obtained ones.

Keywords: X-ray imaging, colour centres, photoluminescence, lithium fluoride, radiation detectors

Riassunto

Recentemente è stato dimostrato quanto i rivelatori per imaging a radiazione basati su centri di colore (CC) luminescenti nel fluoruro di litio (LiF) siano affidabili, efficienti, e con alta risoluzione spaziale su grande area. In questo rapporto tecnico, si verifica la bontà di cristalli e film di LiF come rivelatori per l'imaging in campo quasi lontano di raggi X polienergetici. Le informazioni d'intensità e di fase di un test pattern vengono registrate, sotto forma di distribuzione spaziale di CC, in un rivelatore a lastra di LiF; tali informazioni sono in seguito recuperabili eccitando la lastra con luce blu e fotografando l'immagine di fotoluminescenza (FL) in un microscopio ottico. Si è sviluppato un modello teorico per descrivere l'interazione dei raggi X col test pattern e la formazione nel LiF di CC a causa di irraggiamento X. Infine, sono messi a confronto alcuni dettagli delle mappe di FL calcolate e sperimentali.

Parole chiave: Imaging a raggi x, centri di colore, fotoluminescenza, fluoruro di litio, rivelatori di radiazione

INDEX

1. Introduction	7
2. Colour-centre formation by X-irradiation	8
2.1 Spectral absorption profile	9
2.2. Total absorption profile	9
2.3 Rate of deposited-energy density	10
2.3.1 Absorbed dose	11
2.4 Colour-centre density and photoluminescence	13
3. X-ray quasi-far-field imaging: model and experiment	14
3.1 Interaction with the test pattern and propagation to the LiF detector	17
3.2 Source-size correction	18
3.3 Best fit of the photoluminescence profile	18
3.4 Discussion	22
4. Conclusion	23
References	25

1 Introduction

Insulating materials containing point defects [1] can be successfully utilised as radiation detectors [2]. Colour centres (CC's) [3] in lithium fluoride (LiF) are known for their application in dosimeters [4], miniaturised light-emitting devices [5], and tuneable solid-state lasers [6]. Some of these CC's are optically active and stable at room temperature, with broad absorption and emission bands in the visible spectral range [7]. Aggregate F_2 and F_3^+ centres, consisting of two electrons bound to two and three close anion vacancies, respectively, emit in the red (F_2) and green (F_3^+) parts of the spectrum and have almost overlapping absorption bands (M band) peaked at the wavelength of ~ 450 nm [7]. For this reason, F_2 and F_3^+ centres can be simultaneously excited with a single-wavelength optical pump in the blue.

Due to their high-penetration properties, X-rays are widely used to analyse the internal structure of objects and biological samples. Absorption contrast is the most intuitive and common technique utilised to record radiographies of samples, when these present details whose absorption properties are clearly distinguishable at the operating X-ray wavelengths. However, for high-energy X-rays, the absorption coefficient of most materials is very small and low-atomic-number samples, such as biological ones, behave as phase objects. In such cases, the lack of absorption contrast can be compensated by adding phase information to the recorded image [8]. A possible approach is in-line phase-contrast imaging [8, 9].

High-resolution X-ray imaging can be accomplished with a variety of methods [10]; all of them are limited by the resolution and/or the dynamic range of the detectors. However, novel solid-state LiF radiation detectors, based on the material radiation-sensitivity and optical readout of photoluminescence (PL) from F_2 and F_3^+ CC's, can overcome the above-mentioned limitations so that they are suitable for the characterisation of micro and nanostructures as well as biological samples. Their high spatial resolution across a large field of view, wide dynamic range, and versatility make them very attractive and promising as recording plates for X-ray absorption-contrast [11–14] and phase-contrast [15] imaging.

Suitability of LiF, either in bulk or thin film form, as imaging detector for poly-energetic X-rays was recently tested at the ANKA light source of the KIT synchrotron facility in Karlsruhe, Germany [15]. The test consisted of transmitting the poly-energetic (6–60 keV) X-ray collimated beam through a test pattern, and exposing a LiF detector, placed in the far field, to the transmitted beam. Optically-active CC's are created, in this way, within a superficial layer of LiF, whose depth distribution depends on the energetic spectrum of the X-rays, and with a transversal distribution that reproduces the diffracted shadow of the test pattern. Without any further treatment or special handling, the stored CC distribution can be conveniently detected and acquired as a bi-dimensional map of visible PL in a fluorescence microscope, by illuminating the exposed LiF sample with blue light in order to optically pump F_2 and F_3^+ CC's. A careful comparison of the obtained CC luminescence maps with those generated by simulating the irradiation and readout processes suggests, for the considered doses, that an approximately linear dependence of the CC volume density on the deposited energy is not completely suitable, and that some sort of saturation effect has to be taken into account.

This technical report is organised as follows. In sec. 2, the theory of photon absorption in a solid is briefly recalled, and is applied to evaluate the energy deposited into a solid by a beam of poly-energetic X-rays. Equations are introduced (sec. 2.4) for the estimation of the volume density of CC's that are created in LiF as a consequence of X-irradiation; saturation effects at

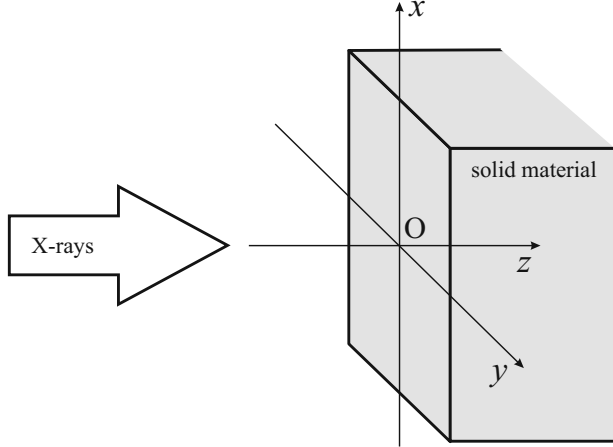


Figure 1. Scheme of the Cartesian coordinate system used for the model. The origin O is placed on the flat external surface of the solid material. The z-axis points towards the interior of the material. The X-rays impinge normally onto the material surface from the negative-z half-space.

high irradiation doses are taken into account in an elementary way. Then, a simple relationship is tentatively assumed for the intensity of PL radiated by optically-pumped CC's. In sec. 3, the interaction of the X-ray wavefront with a test pattern and its subsequent free-space propagation to a LiF detector are dealt with; the opportunity to use either a single-step transmission function or a beam-propagation-method algorithm is discussed. A proper correction is applied to the beam intensity impinging on the detector plane to account for the finite size of the X-ray source, with an estimation of the actual source size; the energy deposited inside the detector and the intensity of PL from CC's therein generated are then calculated. Section 3.3 is dedicated to comparing experimental PL measurements with corresponding model expectations, both for a LiF crystal and a film over glass substrate.

2 Colour-centre formation by X-irradiation

Irradiation of LiF with an X-ray beam generates CC's as a consequence of the energy that X-rays deposit in the material. In a first approximation, for doses well below saturation, one can assume the density of generated CC's to be locally proportional to the density of the deposited energy, which in turn depends on the intensity of X-rays at the considered position and on the irradiation time. The local rate $\dot{\varepsilon}$ of deposited-energy density can be evaluated by using the classical laws of absorption for photons crossing a material. Here, the spatial distribution of $\dot{\varepsilon}$ is estimated for a plane-parallel beam of X-rays normally impinging of the flat surface of a solid material. Assuming the material to be homogeneous, let us identify a position inside it by the depth coordinate z , which is set to $z = 0$ at the material surface and increases inside the material—see fig. 1 for a scheme of the irradiation setup and the coordinate reference system. The z-axis is perpendicular to the surface and its positive direction points inside the material. The rate of deposited-energy density *vs.* the position (x, y, z) —with $z \geq 0$ —is the quantity being looked for.

2.1 Spectral absorption profile

For the majority of materials, reflection of a beam of X-rays that impinges normally onto their surface is extremely low and can be safely neglected.¹ Therefore, the intensity transmittance of a photon of energy E through a space interval of thickness z is given by the well known Lambert-Beer's law [17],

$$T(E, z) = \exp [-\alpha(E)z], \quad (2.1)$$

where $\alpha(E)$ is the material absorption coefficient at the photon energy. The intensity absorbance of the same space interval of thickness z is

$$A(E, z) = 1 - T(E, z) = 1 - \exp [-\alpha(E)z]. \quad (2.2)$$

An impinging photon is absorbed within the infinitesimal spatial range $[z, z + dz]$, *after* crossing the finite spatial range $[0, z]$, with probability

$$p(E, z) dz = T(E, z) A(E, dz). \quad (2.3)$$

The previous equations allow calculating the *linear density of probability* that a photon of energy E is absorbed exactly at the depth z , that is, only *after* it has crossed the above-standing $[0, z]$ layer of material. The linear density of probability is

$$p(E, z) = \alpha(E) \exp [-\alpha(E)z]. \quad (2.4)$$

This quantity is also defined as the *spectral* absorption profile of mono-energetic photons in the material.

One can easily verify that, excluding the trivial case $\alpha(E) = 0$,

$$\int_0^{+\infty} p(E, z) dz = 1 \quad (2.5)$$

holds true, suggesting that an impinging photon is going to be certainly absorbed within a material of infinite extension.

2.2 Total absorption profile

Now, let us consider an impinging *poly-energetic* X-ray beam. In order to count *all* the photons that get absorbed at the depth z , one should integrate eq. (2.4) over E , provided a suitable weight factor, corresponding to the spectral energy distribution of the beam, is applied. The result, let us name it $P(z)$, can be defined as the *total* absorption profile of photons and will depend on z only.

Let us assume that the *spectral* flux $\Phi_X(E)$ of the impinging beam is known, where $\Phi_X(E) dE$ is the number of photons of energy between E and $E + dE$ that cross the unit surface per unit time. For the moment, the flux is assumed to be homogeneous over the plane (x, y) . The *total* flux is the energy integral of $\Phi_X(E)$, that is

$$\Phi_{X_{TOT}} = \int_0^{\infty} \Phi_X(E) dE. \quad (2.6)$$

¹For instance, in case the material is LiF, normally impinging X-rays of energies larger than 6 keV (see sec. 3) have a reflection coefficient $R < 10^{-11}$ [16].

As one might expect, $\Phi(E)/\Phi_{X_{TOT}}$ represents the weight needed to calculate $P(z)$. It ensues

$$P(z) = \frac{1}{\Phi_{X_{TOT}}} \int_0^\infty p(E, z) \Phi_X(E) dE. \quad (2.7)$$

$P(z) dz$ is the fraction of photons of *whatever energy* that are absorbed between z and $z + dz$ after crossing the spatial range $[0, z]$. The total absorption probability is

$$\int_0^{+\infty} P(z) dz = 1, \quad (2.8)$$

which is the normalisation condition that any probability density distribution must obey; its meaning is that photons are going to be sooner or later absorbed while propagating inside an infinitely extended material.

In case the X-rays are mono-energetic, the above eq. (2.7) holds still good, provided the normalised flux $\Phi_X(E)/\Phi_{X_{TOT}}$ is replaced by a Dirac-delta distribution centred around the photon energy.

2.3 Rate of deposited-energy density

The *spectral* intensity of the X-ray beam can be defined as

$$I_X(E) = \Phi_X(E) E. \quad (2.9)$$

The quantity $I_X(E) dE$ represents the energy fraction, per unit time and crossed surface, carried by photons having energies between E and $E + dE$. Here, this quantity is evaluated at the material surface $z = 0$, that is, just before crossing it (see fig. 1). It follows that the *total* intensity of the impinging beam is

$$I_{X_{TOT}} = \int_0^\infty I_X(E) dE. \quad (2.10)$$

As one can verify from the previous results, $p(E, z) \Phi_X(E) dE dx dy dz$ is the number of photons of energies between E and $E + dE$ that, per unit time, are absorbed within an infinitesimal cube $dx dy dz$ at the depth z within the material, after crossing the above-standing material layer $[0, z]$. Therefore, $p(E, z) I_X(E) dE dx dy dz$ is the energy deposited per unit time in the infinitesimal cube by those photons whose energies are in the range $[E, E + dE]$. It follows that the energy density that is deposited per unit time (rate of deposited-energy density), $\dot{\varepsilon}$, at the depth z is the above quantity divided by the cube volume $dx dy dz$ and integrated along E , that is

$$\dot{\varepsilon}(z) = \int_0^\infty p(E, z) I_X(E) dE = \int_0^\infty \alpha(E) \exp[-\alpha(E)z] I_X(E) dE. \quad (2.11)$$

For the sake of simplicity and in view of the applications in the following of the present work, the intensity $I_X(E)$ is assumed to be time-invariant—therefore, also $\dot{\varepsilon}(z)$ is time-invariant.

For mono-energetic X-rays of energy E and intensity I_X ,² the previous equation simplifies to

$$\dot{\varepsilon}(z) = \alpha \exp(-\alpha z) I_X. \quad (2.12)$$

²Rigorously speaking, such a mono-energetic beam possesses a Dirac-delta distributed *spectral* intensity equal to $I_X \delta(E' - E)$, therefore the *total* intensity is $I_{X_{TOT}} = I_X \int_0^\infty \delta(E' - E) dE' = I_X$. However, for simplicity, the word “intensity” will be used in this case without the adjective spectral or total, unless it is necessary to explicitly make such a distinction.

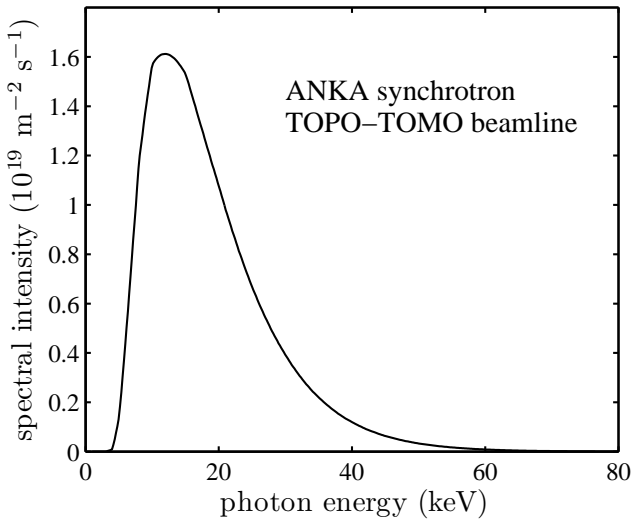


Figure 2. Spectral intensity of the TOPO-TOMO beamline at the ANKA light source (Institute for Synchrotron Radiation, Karlsruhe Institute of Technology KIT, Germany), as transmitted through a $500\text{ }\mu\text{m}$ thick Be-window, normalised according to ref. [15]. Note that the ordinate units include no energy units, because the *spectral* intensity $I_X(E)$ is defined in such a way that actually $I_X(E) dE$ is the amount of energy, per unit time and crossed surface, carried by photons of energy between E and $E + dE$ —see eqs. (2.9) and (2.10).

It can be verified that

$$\int_0^{+\infty} \dot{\varepsilon}(z) dz = I_{X_{TOT}}, \quad (2.13)$$

in agreement with energy conservation, both for the poly-energetic and the mono-energetic case.³

Finally, if t is the irradiation time, the deposited-energy density profile at z is simply

$$\varepsilon(z) = \dot{\varepsilon}(z) t. \quad (2.14)$$

2.3.1 Absorbed dose

Recalling that the *absorbed dose*, D , is the energy absorbed per unit mass [18], one easily recognises that D must be proportional to ε . Indeed, according to its definition, D can be calculated by dividing ε by the mass density ρ —which can be a position-dependent quantity, in case the material is non-homogeneous⁴—of the irradiated material,

$$D(z) = \frac{\varepsilon(z)}{\rho(z)}. \quad (2.15)$$

³See note 2.

⁴However, in such a case, also the absorption coefficient of the material is likely to be spatially dependent, so that the expression of $\dot{\varepsilon}$ in eq. (2.11) should be corrected accordingly.

Let us consider the *white*—that is, poly-energetic—X-ray beam of the TOPO-TOMO beamline at the ANKA light source (Institute for Synchrotron Radiation, Karlsruhe Institute of Technology KIT, Germany), on which our attention will be focused again later in this work. The *nominal* beam-flux value at sample position is $\sim 10^{16}$ ph/s across an area of 1 cm^2 [19]. For the setup that is considered in sec. 3, which includes photon propagation in air and transmission through a $500\text{ }\mu\text{m}$ thick Be window, the beam-flux is lowered to $\sim 2 \times 10^{15}\text{ ph s}^{-1}\text{cm}^{-2}$ [15]. Using the spectral distribution of the transmitted beam at sample position [15], shown in fig. 2, and the optical constants of LiF [16], one can estimate the absorbed dose in LiF ($\rho = 2.635\text{ g/cm}^3$) per unit time along z by means of eqs. (2.11), (2.14) and (2.15). The theoretical absorbed dose of a LiF sample placed at the sample position of the beam is shown in fig. 3. It features a quasi-exponential-decay behaviour along z —an actual exponential-decay curve⁵ is shown in the same figure for comparison—and can be useful to estimate not only the z -dependence of the absorbed dose, but also its amount (normalised to the flux), which is proportional to the irradiation time.

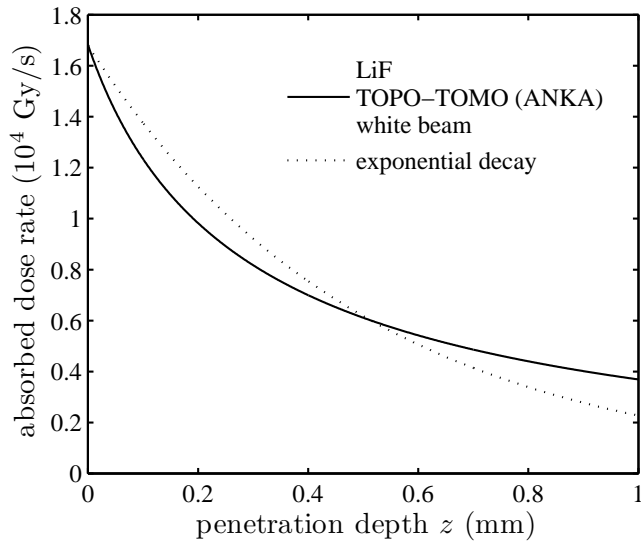


Figure 3. Estimated absorbed dose *per unit time* in LiF vs. penetration depth (z axis, see fig. 1). The evaluation has been made by using the flux value $2 \times 10^{15}\text{ ph/s}$, across an area of 1 cm^2 [15], of the white-beam TOPO-TOMO line of the ANKA light source (Institute for Synchrotron Radiation, Karlsruhe Institute of Technology KIT, Germany), and the spectral intensity distribution shown in fig. 2. An exponential-decay curve—see note 5—is also shown for comparison.

It should be pointed out that tabulated data of LiF optical constants we have access to are available only up to 30 keV [16], a value lower than the upper limit (~ 60 keV) of the beam energy distribution shown in fig. 2, so that the numerical integration needed to calculate $\dot{\varepsilon}(z)$, see eq. (2.11), had to be truncated at that value. For this reason, one is legitimated to wonder whether the absorbed dose plotted in fig. 3 is underestimated. This is actually true, but the underestimation *is likely* to be almost negligible for depth values up to $z \sim 200\text{ }\mu\text{m}$. Let us see why. The attenuation

⁵The exponential function, whose parameters are chosen to make it follow as much as possible the absorbed dose rate curve within the abscissa range, is $1.68 \times 10^4 \exp(-z/0.5)$.

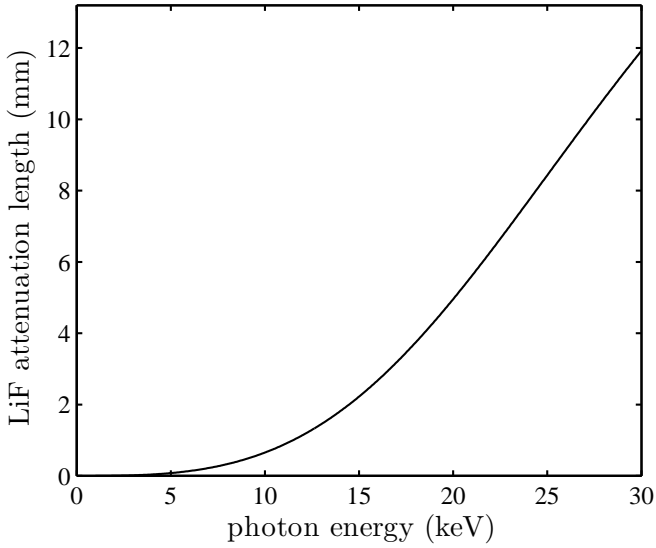


Figure 4. Attenuation length of X-rays in LiF according to the tabulated optical constants available in [16].

length in LiF increases about linearly with photon energy for $E \gtrsim 20$ keV, see fig. 4, and its trend suggests that it could keep increasing also at energies greater than 30 keV. If that is true, the probability $\int_0^{200\text{ }\mu\text{m}} p(E, z) dz$ for a photon of energy $E > 30$ keV to be absorbed—and hence deposit its energy—within the first 200 μm of material is rather small, less than 0.017, as one can verify. Considering also that the portion $E > 30$ keV of the spectrum in fig. 2 represents just a tail of the whole distribution, we are quite confident to assume the dose plot in fig. 3 to be accurate enough for our purposes, at least within the depth interval $0 \leq z \leq 200\text{ }\mu\text{m}$.

2.4 Colour-centre density and photoluminescence

In a tentative linear-model approach, the volume density of CC's generated by ionising radiation could be thought to be proportional to the amount of deposited-energy density ε . This could be approximately true, indeed, for doses that are not too high. However, our first attempts to replicate the experimental data of sec. 3 with such a linear model gave results that were not completely satisfying, thus suggesting the need for a more refined model to relate deposited-energy and CC density. Obviously, the density of CC's cannot grow indefinitely, therefore saturation should occur above a certain dose threshold. If a suitable saturation mechanism is included in the model so that the experimental data of sec. 3 are satisfactorily reproduced, it is highly probable that those data correspond to doses close or above the threshold separating linearity from saturation.

The simplest “upgrade” from the linear-model approach consists of neglecting particular recombination mechanisms in the defect formation process that are responsible for nonlinearities [20–22] and adopting the elementary differential equation, introduced by Soshea and co-workers to describe the formation of CC's in MgO [23], where the possibility is included that ionising radiation

can mediate, besides creation, also annihilation of CC's,

$$\frac{dN}{dt} = \beta\dot{\varepsilon} - \gamma\varepsilon N. \quad (2.16)$$

Here, N is the volume density of CC's of a certain kind, while β and γ are two parameters of suitable dimensions, assumed to be both time-invariant and energy-invariant, which regulate defect creation and annihilation, respectively. Assuming null zero-time centre density, $N(0) = 0$, and recalling that $\varepsilon \equiv \dot{\varepsilon}t$, the solution to this differential equation gives the simplest, yet saturation-wise, relationship between CC density and deposited-energy density,

$$N = N_{\max} [1 - \exp(-\gamma\dot{\varepsilon}t)] \equiv N_{\max} [1 - \exp(-\gamma\varepsilon)], \quad (2.17)$$

with $N_{\max} \equiv \beta/\gamma$. Note how, as expected, an elementary linear dependence $N \simeq \beta\varepsilon$ is recovered for values of the deposited-energy density so small that $\gamma\varepsilon \ll 1$.

Because, as explained in sec. 2.3, the deposited-energy density ε is a function of depth z inside LiF, also the densities of F_2 and F_3^+ CC's should depend on z . Assuming the intensity of the optical pump, utilised to excite the CC's, to be well below saturation, the PL amount that can be extracted from X-irradiated LiF should be proportional to the total number of centres within the optically pumped volume.⁶ Considering the PL emitted by aggregate CC's that are located within a certain surface layer $0 \leq z \leq Z$ of LiF, one can expect the PL intensity due to each kind of them to be

$$I_{\text{PL}} = \int_0^Z q(z)N(z) dz, \quad (2.18)$$

where $q(z)$ is a suitably dimensioned function that accounts for the pump characteristics and the quantum efficiency of the process, plus other possible inhomogeneities along z .

Under the simplifying condition that $q(z)$ can be approximated with its average in $0 \leq z \leq Z$, $q(z) \simeq \bar{q}$, and by substituting eq. (2.17) into eq. (2.18), one finds

$$I_{\text{PL}} = \bar{q}N_{\max} \left\{ Z - \int_0^Z \exp[-\gamma\dot{\varepsilon}(z)t] dz \right\}. \quad (2.19)$$

This is the expression for the PL intensity we are going to use in sec. 3 to compare experimental results with theory, with $\dot{\varepsilon}(z)$ given by eq. (2.11).

3 X-ray quasi-far-field imaging: model and experiment

As an application of the theoretical model introduced in sec. 2, the reproduction of two experimental PL profiles is here addressed. These profiles were measured at a confocal microscope operated in fluorescence mode by illuminating with blue light the diffraction images of a test pattern recorded, respectively, on a LiF crystal and a film as local distributions of CC's. The crystal thickness was 1 mm, while the film was grown on a glass substrate by thermal evaporation (10^{-4} Pa vacuum pressure) at the ENEA laboratories of Frascati [15, 24]—its thickness amounted to 1 μm .

⁶In case the pump intensity is not constant along z , a suitable weighting function has to be introduced.

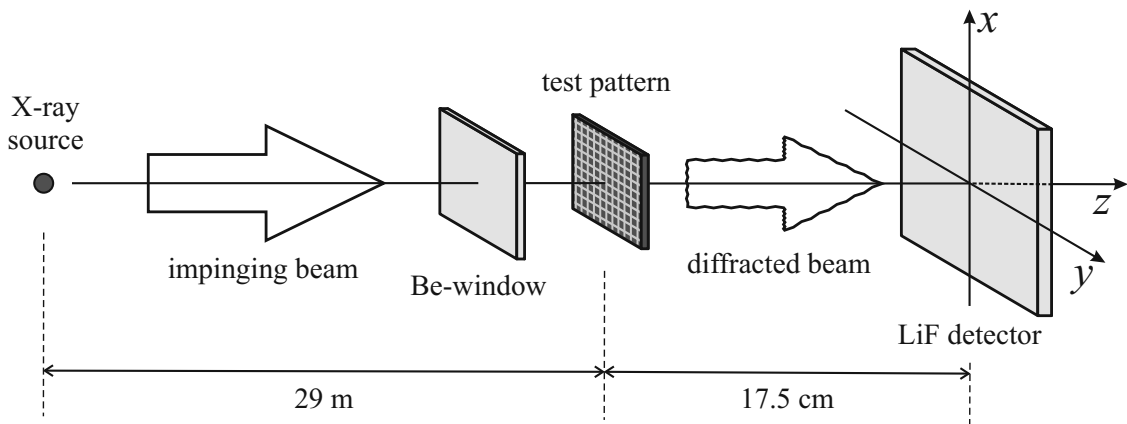


Figure 5. Simplified scheme of the irradiation setup in the quasi-far-field X-ray imaging experiment on LiF detector at the TOPO-TOMO beamline of the ANKA light source (Institute for Synchrotron Radiation, Karlsruhe Institute of Technology KIT, Germany).

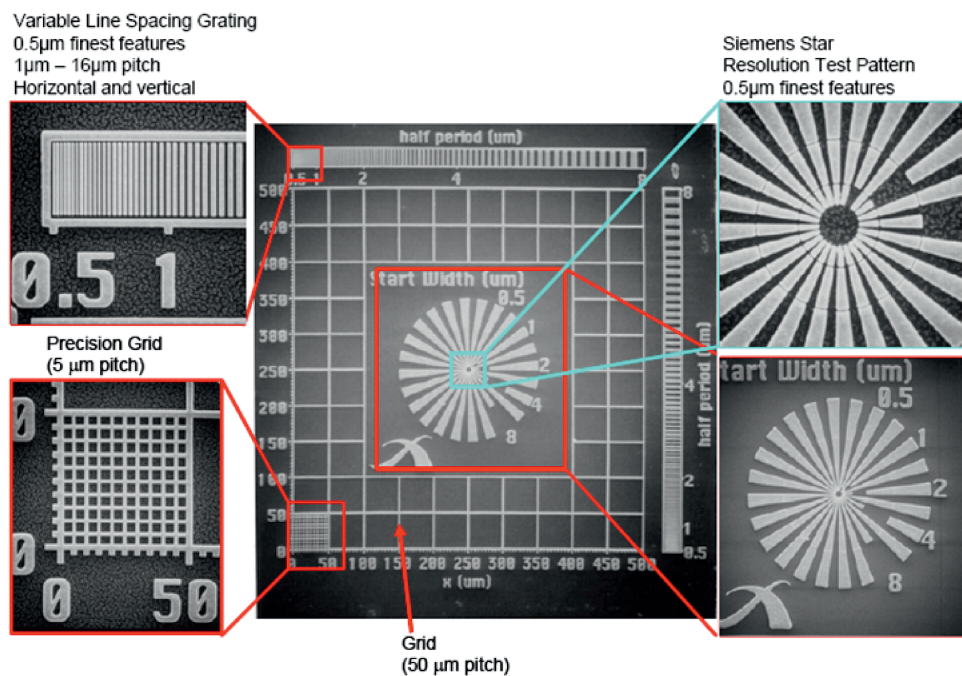


Figure 6. Features of the Xradia X500-200-30 (Xradia, Pleasanton, CA, USA) test pattern that was utilised in the quasi-far-field X-ray imaging experiment on LiF at the TOPO-TOMO beamline of the ANKA light source (Institute for Synchrotron Radiation, Karlsruhe Institute of Technology KIT, Germany).

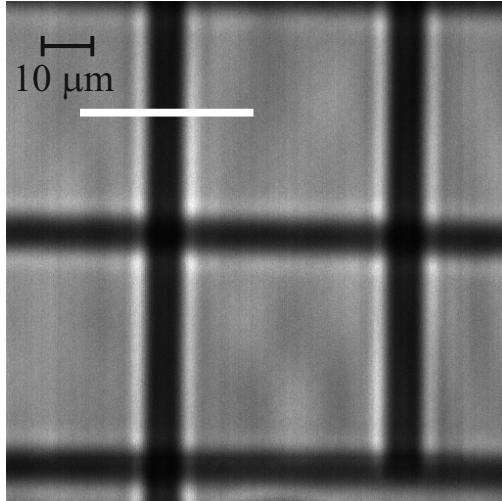


Figure 7. Particular of the PL map read from the X-ray-exposed LiF film [15]. The white line indicates the path along which the PL profile Anka3 was scanned for further analysis.

The LiF crystal and film were used as detectors for a quasi-far-field imaging experiment performed at the TOPO-TOMO beamline of the ANKA light source (Institute for Synchrotron Radiation, Karlsruhe Institute of Technology KIT, Germany) [15]. An Xradia X500-200-30 (Xradia, Pleasanton, CA, USA) test pattern was placed across the poly-energetic X-ray beam after this latter had been transmitted through a 500 μm thick polished Be-window (6 keV to about 60 keV, see fig. 2) and then through the test pattern, see figs. 5 and 6. The presence of the Be-window between the light source and the test pattern was properly taken into account; it exerted an attenuation of beam so that the photon flux that impinged onto the test pattern was estimated to be $\sim 2 \times 10^{15} \text{ ph s}^{-1} \text{ cm}^{-2}$. The LiF crystal and film were exposed for $t = 30 \text{ s}$, under identical conditions, to the diffracted X-ray beam at a distance of 17.5 cm from the test pattern. In this way they were exposed to the X-ray diffracted image of the test pattern, in which the intensity and phase pieces of information of the latter were embedded [25].

Two PL intensity profiles were measured with a confocal microscope (Nikon Eclipse 80i-C1) operating in fluorescence mode: one profile was measured on the exposed LiF crystal (sample name: Anka2), the other one on the exposed LiF film on glass substrate (sample name: Anka3). The confocal microscope utilises a blue-light (457.9 nm continuous-wave argon laser) optical pump to excite the optically active CC's in the examined sample, and detects the spectrally-integrated radiated PL as a bi-dimensional image that is recorded by a CCD camera [15]. If needed, optical filters can provide a separation of the red and green parts of the spectrum in the detection process. Later, the digitised image is scanned along the desired direction to get a mono-dimensional intensity profile.

The examined PL profiles are scans of the test-pattern diffracted images that were recorded—as local concentrations of CC's—on the LiF detectors. The path of one of the profiles—the one corresponding to the LiF film—scanned perpendicularly to a detail of the test pattern consisting of a tiny rail forming the larger pattern grid, is shown in fig. 7.

In this way, experimental PL intensity profiles were acquired along a common scanning direction (the x -axis, to fix ideas). They are being compared in the following to their theoretically estimated counterparts.

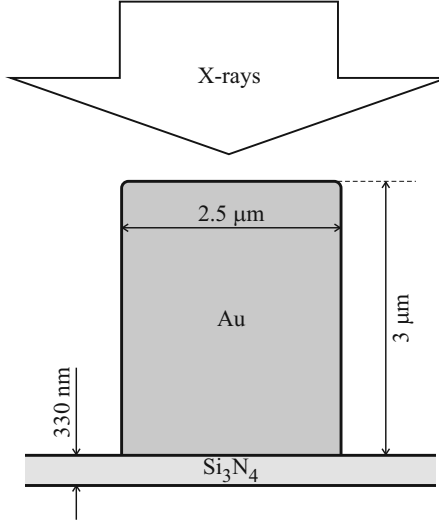


Figure 8. Cross-section of the test-pattern detail that was considered for the simulations: a microscopic gold rail placed over a Si_3N_4 plate. See the text for further details.

3.1 Interaction with the test pattern and propagation to the LiF detector

The detail of the test pattern that is covered in the scanned profiles consists of a microscopic gold rail, $h_{\text{Au}} = 3 \mu\text{m}$ high and $2w_{\text{Au}} = 2.5 \mu\text{m}$ wide, placed over a Si_3N_4 plate of thickness 330 nm, see fig. 8. To avoid the unrealistic perfectly sharp corners of a rectangle that could spoil the X-ray diffraction numerical evaluation, the transverse section of the rail (plane Oxz) was simulated with a super-Gaussian curve, $h_{\text{Au}} \exp [- (|x| / w_{\text{Au}})^{n_{\text{SG}}}]$, with super-Gaussianity order $n_{\text{SG}} = 10^4$. As shown in fig. 5, the X-rays impinge along the z -axis onto the structure, are transmitted through it, then propagate for 17.5 cm until they reach the LiF detector, which lies over the Oxy plane. The following simulations assume, for the sake of simplicity, diffraction along the x -axis only (two-dimensional approximation), and infinite extension of the rail along the y -direction. The impinging radiation is supposed to be a poly-energetic plane-wave with wavevector parallel to z , and energy distribution as specified in ref. [15] and shown in fig. 2. The optical constants of the materials at the X-ray energies are those reported in the webpage of the Centre for X-ray Optics of the Berkeley Laboratories [16].

At the considered energies, the gold rail thickness corresponds to a large number of X-ray wavelengths, which span the range $0.4\text{--}12.4 \text{\AA}$.⁷ For this reason, transmission of the X-ray wavefront through the gold rail and the Si_3N_4 plate along z was calculated in two ways: (a) by simply multiplying the impinging wavefunction by a global amplitude-transmittance function, and (b) by utilising the improved beam propagation method (IBPM) [27] to more rigorously address the wavefront transmission problem. The results of the two methods were later compared: the former approach,

⁷Use of the term *quasi-far-field* is due to the dimensions involved in the experiment. Far-field nominally corresponds to a distance that can be considered much larger than the Fraunhofer distance. Because the Fraunhofer distance is defined as $d_F \equiv a^2 / \lambda$ [26], where a is the lateral size of the detail being diffracted (classically, a slit width), one can verify that, for the considered sample ($a \equiv 2w_{\text{Au}} = 2.5 \mu\text{m}$) and poly-energetic beam ($0.4 \text{\AA} \leq \lambda \leq 12.4 \text{\AA}$), the Fraunhofer distance spans the range $0.5 \text{ cm} \leq d_F \leq 15.5 \text{ cm}$ according to the considered wavelength. Therefore, the free-space propagation distance of 17.5 cm can mean far-field for some wavelengths of the beam, near-field for some others. It is, however, not fully far-field for the $\sim 12 \text{ keV}$ spectral-intensity peak (see fig. 2), to which the Fraunhofer distance $d_F \simeq 6.1 \text{ cm}$ corresponds.

simpler and less lengthy, resulted to be accurate enough to calculate the wavefront transmitted by the structure.

Finally, free-space propagation of the X-ray wavefront from the test pattern exit plane to the LiF detector surface was evaluated in the Fourier space [28, 29] by using the Fast Fourier Transform (FFT) libraries of MATLAB [30], in whose environment all the simulations reported in this work were performed.

3.2 Source-size correction

The Xradia X500-200-30 (Xradia, Pleasanton, CA, USA) test pattern was distant $z_1 = 29$ m from the source of the TOPO-TOMO beamline (see fig. 5). After passing through the test pattern, the X-ray beam propagated for other $z_2 = 17.5$ cm before reaching the LiF detector. Because the size of the source is non-zero, the transversal coherence of the beam is not infinite [31, 32]. For this reason, the intensity I_X of the X-ray beam at the LiF surface ($z = 0$), needed to calculate the rate of deposited-energy density inside the detector material—see eqs. (2.9) and (2.11)—has to be suitably corrected.

A way to achieve the corrected intensity consists of a two-step process: first, X-ray propagation from the source up to the LiF detector, passing through the test pattern, is calculated by temporarily assuming full transversal coherence; then, the resulting fully-coherent intensity on the LiF surface is convoluted with a properly scaled version of the source distribution function (SDF) [9, 33]. Assuming, for simplicity, a Gaussian SDF,

$$S_0(x) \equiv \exp\left(-\frac{x^2}{2\sigma_0^2}\right), \quad (3.20)$$

the scaled SDF is

$$S(x) \equiv S_0\left(\frac{z_1}{z_2}x\right). \quad (3.21)$$

The full-width at half-maximum (FWHM) of a Gaussian curve like $S_0(x)$ is approximately $2.35\sigma_0$. This value has to match the lateral extension of the source, which is nominally a $800\text{ }\mu\text{m} \times 200\text{ }\mu\text{m}$ rectangle⁸ [19]. Therefore, $2.35\sigma_0$ can be expected to be valued between $200\text{ }\mu\text{m}$ and $800\text{ }\mu\text{m}$, depending on the orientation of the scanned segment (fig. 7) with respect to the source, plus other factors.

After the X-ray intensity $I_X(x)$ —normalised as in fig. 2—impinging on the LiF surface has been corrected for the finite size of the source by convoluting it with $S(x)$, it can be inserted in eq. (2.11) to calculate the rate of deposited-energy density ε in a more correct way.

3.3 Best fit of the photoluminescence profile

The theoretical model of sec. 2 was utilised to best fit experimental PL profiles obtained by scanning at the optical microscope CC maps recorded with the above described quasi-far-field imaging setup.

⁸Those lengths correspond to the FWHMs of the source intensity along the horizontal and vertical direction, respectively.

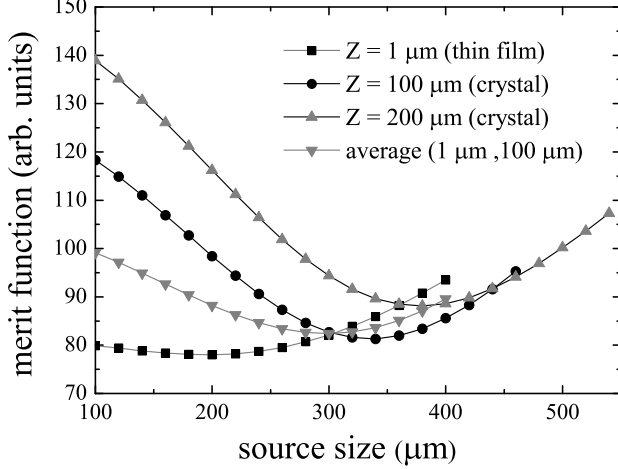


Figure 9. Merit-function values *vs.* source size ($2.35\sigma_0$) for the cases of crystal and thin film. For the crystal, the plots corresponding to two different values of the optically-pumped thickness Z are shown. See the text for further details.

Because we are dealing with PL profiles along the x -axis, let us rewrite eq. (2.17) by making explicit the dependence on x of the involved parameters. Moreover, let us introduce three convenient fit parameters— p_1 , p_2 and p_3 . The resulting expression for the PL intensity is

$$I_{\text{PL}}(x) = p_1 \left\{ Z - \int_0^Z \exp [-p_2 \dot{\varepsilon}(x - p_3, z)] dz \right\}. \quad (3.22)$$

The first two parameters, $p_1 \equiv \bar{q}N_{\max}$ and $p_2 \equiv \gamma t$, are assumed to be sample-dependent because of the peculiar structure that each LiF film or crystal can have; therefore, they are not forced to assume identical values for distinct samples. The same holds true for the third parameter, p_3 , which acts as a shift operator along x and is used to align each theoretical PL profile to its experimental counterpart. It is worth mentioning that p_1 also includes a scale factor, non explicitly written to keep notation simple, used to properly scale theoretical intensity data to the arbitrary units used for measured data.

Data elaboration started by estimating an optimal source size $2.35\sigma_0$ that should be common to each measurement. To that purpose, a MATLAB [30] best-fit program was developed, whose output is a theoretical PL intensity profile made as close as possible to the input experimental one by varying the three fit parameters. The distance between the experimental and theoretical intensity profiles is quantified by means of a classical root-mean-square merit function, which assumes a minimum value when the experimental and theoretical points are as close as possible. For the crystal only, several values Z of the optically-pumped thickness were tested, showing that the best results, in terms of merit function, are obtained for $Z \simeq 100\mu\text{m}$ —the fact that Z is smaller than the crystal thickness is very likely ascribable to the limited z -range of the focused optical pump. For the film, the value of Z was set to exactly coincide with the film thickness, $Z = 1\mu\text{m}$.

Figure 9 displays the obtained optimal merit-function figures *vs.* source-size values—only the best two among several tested Z values for the crystal are shown. As anticipated, $Z = 100\mu\text{m}$ represents the best optically-pumped depth for the crystal. The plots demonstrate that while $2.35\sigma_0 = 200\mu\text{m}$ is the optimal source size for the LiF film, the merit function corresponding to the LiF crystal (with $Z = 100\mu\text{m}$) has a minimum at about $2.35\sigma_0 = 340\mu\text{m}$. A trade-

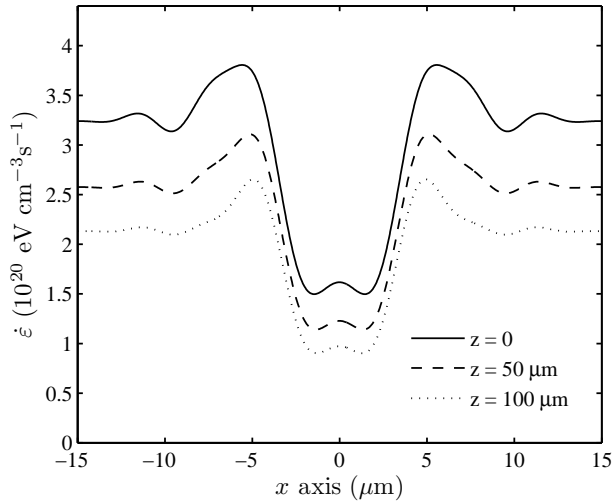


Figure 10. Theoretical x -profiles of the rate $\dot{\epsilon}$ of deposited-energy density in LiF at the surface ($z = 0$) and at two depth values ($z = 50 \mu\text{m}$ and $z = 100 \mu\text{m}$), as due to the quasi-far-field (17.5 cm) diffraction of the poly-energetic TOPO-TOMO X-ray beam through the Xradia X500-200-30 test pattern.

off curve, obtained as the mathematical average between the film and the crystal ($Z = 100 \mu\text{m}$) curves, can be calculated; it is shown in fig. 9 as well, featuring a minimum at $2.35 \sigma_0 = 300 \mu\text{m}$. Therefore, this value was chosen as the optimal source size for both the crystal and film cases.

The theoretical x -profiles of the rate $\dot{\epsilon}$ of deposited-energy density in LiF at the surface ($z = 0$) and at two representative depth values ($z = 50 \mu\text{m}$ and $z = 100 \mu\text{m}$), as due to the quasi-far-field (17.5 cm) diffraction of the poly-energetic TOPO-TOMO X-ray beam through the Xradia X500-200-30 test pattern, are plotted in fig. 10. They were calculated by means of eq. (2.11), into which the intensity I_X of the diffracted X-ray field, having spectral distribution as shown in fig. 2, was inserted. I_X was also corrected for the finite size of the X-ray source, $2.35 \sigma_0 = 300 \mu\text{m}$, as explained in sec. 3.2.

The measured PL intensity profiles of samples Anka2 and Anka3 and their corresponding best-fitting theoretical profiles, calculated with eq. (3.22), are shown in figs. 11 and 12, respectively. In both the figures, one notices a fairly good reproduction of the experimental data near the centre, corresponding to the shadow of the gold rail that is projected onto the detector. Outside this central area, the reproduction is slightly worse, especially for Anka3, since the rippled behaviour (enhanced edge contrast) is followed less accurately. An attempt was made to refine the theoretical profiles in those external lobes by taking into account that other rails, parallel to the examined one and spaced $50 \mu\text{m}$ apart—see figs. 6 and 7—are present. With that in mind, the calculation x -domain of the FFT propagation routine was extended to include the closest neighbouring rails, however the results were very close to the ones obtained with the single central rail only and shown in figs. 11 and 12. Perhaps one could get better results by considering that a three-dimensional treatment of the propagation problem should be faced in the $Oxyz$ space instead of the simplified bi-dimensional approach in the Oxz plane, thus including also rails that lie along the x -axis to form a portion of the mesh which is visible in fig. 6. For the film case only, a better agreement could be reached by taking into account interference of the internal multi-reflections both for the optical pump and radiated PL. Such improvements of the model are being targeted in future studies

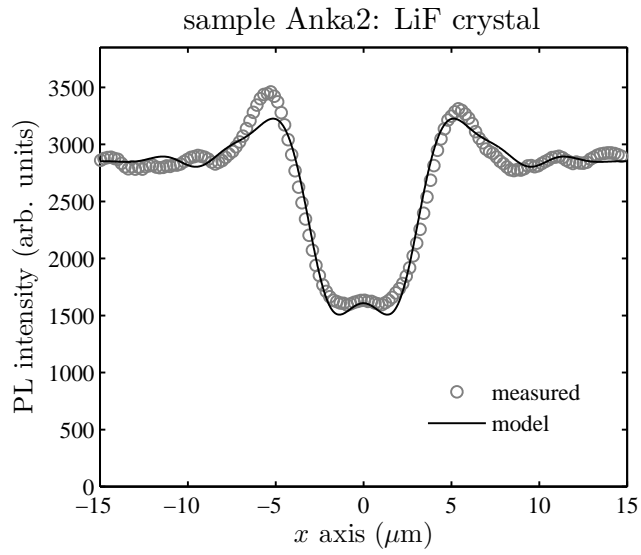


Figure 11. Experimental and theoretical PL intensity profiles due to colour centres formed by X-ray exposition in a LiF crystal of thickness 1 mm (actual optically-active thickness of 100 μm). Irradiation was performed at the TOPO-TOMO beamline of the ANKA light source (Institute for Synchrotron Radiation, Karlsruhe Institute of Technology KIT, Germany) in the framework of a quasi-far-field X-ray imaging experiment using an Xradia X500-200-30 (Xradia, Pleasanton, CA, USA) test pattern. See the text for more details.

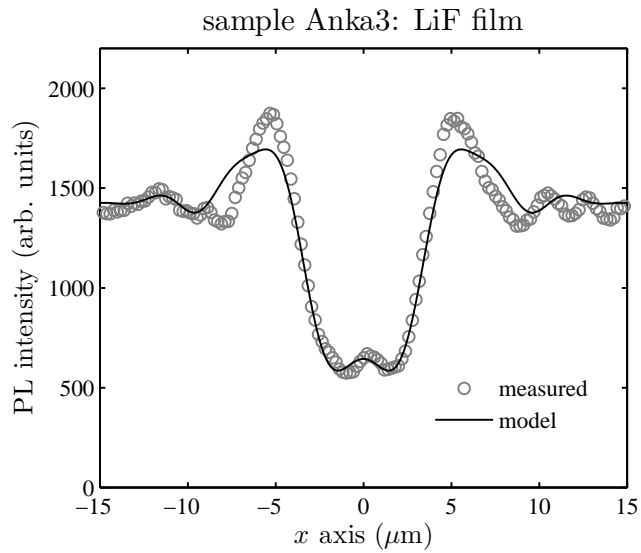


Figure 12. Experimental and theoretical PL intensity profiles due to colour centres formed by X-ray exposition in a LiF film of thickness 1 μm . Irradiation was performed at the TOPO-TOMO beamline of the ANKA light source (Institute for Synchrotron Radiation, Karlsruhe Institute of Technology KIT, Germany) in the framework of a quasi-far-field X-ray imaging experiment using an Xradia X500-200-30 (Xradia, Pleasanton, CA, USA) test pattern. See the text for more details.

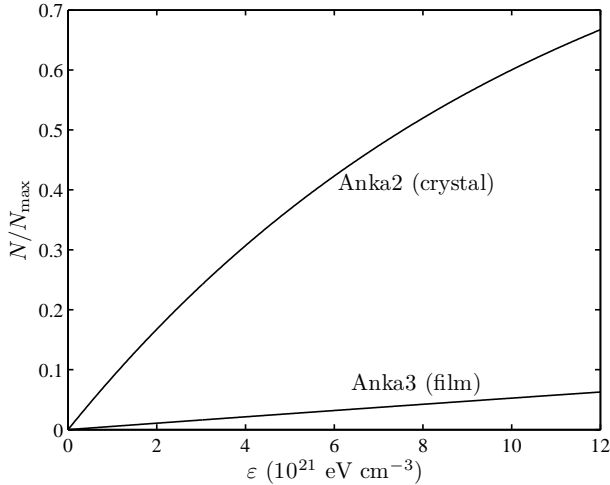


Figure 13. Theoretical normalised volume density of CC’s in the two samples calculated according to the results of the best fit. See the text for more details.

together with the analysis of samples of other shapes and materials.

3.4 Discussion

By comparing figs. 11 and 12, it is worth noting how different “contrast” values of the PL profiles are found for the crystal and the film. As a matter of fact, let us consider the ratio of the PL minimum—located at the centre of the gold rail shadow—to the PL external plateau. As one can verify, this ratio is $\sim 60\%$ for the crystal, and $\sim 40\%$ for the film, thus indicating a better “contrast” for the latter.

SAMPLE	type	p_1 (arb. units)	p_2 ($\text{cm}^3\text{s/eV}$)	p_3 (μm)
Anka2	crystal	56.13	2.75×10^{-21}	15.37
Anka3	film	30811	1.62×10^{-22}	15.02

Table 1. Best-fitting values of the three parameters.

Let us look at the optimal parameter values, listed in tab. 1, that result from the best fitting. The value of p_2 , i.e., γt , is one order of magnitude larger in the crystal than in the film.⁹ Considering that the exposition time to X-rays, $t = 30$ s, was the same for the crystal and for the film, one concludes that γ is much larger in the crystal than in the film. We partially ascribe the above-mentioned different “contrast” values of the PL profiles to this relevant difference in γ , which can be interpreted as a tendency of CC’s in a crystal to be destroyed more quickly than in a film. Indeed, according to eq. (2.16), a larger value of γ means that a smaller value of $\dot{\varepsilon}N$ is needed to get the same negative contribution to dN/dt . In other words, the creation process of CC’s in the crystal seems to saturate earlier than in the film.

⁹Note that the values of p_2 are influenced by the normalisation chosen for I_X . Here we are using the normalisation shown in fig. 2.

This fact is more clearly illustrated in fig. 13. Here, the volume-density ratio N/N_{\max} is calculated by means of eq. (2.17) within a range of deposited-energy density ε that spans the estimated range of $\dot{\varepsilon}$ for the experiment, as shown in fig. 10, multiplied by the irradiation time $t = 30$ s. The two curves have been calculated with γt set to the values of p_2 found from the best-fit process and listed in tab. 1. Note how the volume density of CC's gets close to saturation earlier in the crystal than in the film. This fact could mean that a higher deposited energy is needed for the film to reach the same amount of aggregate CC's as in the crystal (as if aggregate CC's in the film were slower or delayed in forming than in a crystal), and/or that the film can host more F_2 and F_3^+ CC's than the crystal (that is, as if N_{\max} was higher in the film than in the crystal). Previous literature results [34] and some experimental evidence seem to favour the latter hypothesis, even though the former one cannot be completely excluded. This topic surely deserves further studies.

Such conclusions have, for now, to be regarded as speculative ones, at least until further evidence emerges from other analysis, because they are based on just two examined samples and are the result of quite a simplified model and assumptions: for instance, the fact that F_2 and F_3^+ centres can be created with distinct rates of density growth has not been taken into account. It is indeed quite surprising that such a simplified model works decently for such a complex experiment. Work is in progress to perfect the model and test it for other study cases, in order to better describe what actually takes place.

4 Conclusions

The suitability of LiF-based devices as detectors for poly-energetic X-rays has been positively tested. In particular, use of such detectors in quasi-far-field imaging experiments in a synchrotron has been demonstrated. They allow for high resolution storage of an image as a spatial distribution of CC's, which can be comfortably observed at an optical microscope provided the aggregate F_2 and F_3^+ CC's are optically excited with suitable blue light. No development process is needed, and handling is possible even in daylight and at room temperature.

To analyse the results of the above-mentioned tests, an *ad hoc* theoretical model has been developed and implemented in MATLAB [30]. The model starts with evaluating the rate of deposited-energy density by a collimated electromagnetic beam in a solid material. Then, a simplified saturation-wise differential equation is built: it connects the volume density of point defects being created to the deposited-energy density. By applying it to CC's in LiF, the resulting density distribution of optically-active CC's can be evaluated and, consequently, the intensity of radiated PL estimated. Such results have been eventually applied to the X-ray diffraction setup of a recent synchrotron experiment, where the collimated poly-energetic X-ray beam was transmitted through an Au-Si₃N₄ test pattern and free-propagated till a LiF-based detector in the quasi-far-field; the diffracted beam "impresses" a stable spatial distribution of CC's in the detector, whose luminescence can be later read and mapped at high definition with a suitably equipped optical microscope.

Experimental profiles of PL that were read out on such detectors, both in crystal and film form, have been compared to their corresponding theoretical counterparts, obtained from the above-described theoretical model. Even though the agreement between experiment and theory is far from being perfect, it is quite satisfying, especially in the areas corresponding to the most absorbed X-ray intensity. Future experiments and studies are being planned to improve imaging capabilities as far as usability of LiF-based devices and their theoretical design are concerned.

References

- [1] Ashcroft N W and Mermin N D 1981 *Solid State Physics* (Philadelphia: Holt-Saunders International Editions)
- [2] Shionoya S and Yen W M 1998 *Phosphor Handbook* (Boca Raton: CRC Press)
- [3] Fowler W B 1968 *Physics of Color Centers* (New York: Academic Press)
- [4] Lakshmanan A R, Madhusoodanan U, Natarajan A and Panigrahi B S 1996 *phys. stat. sol. (a)* **153** 265–273
- [5] Montereali R M 2002 Point defects in thin insulating films of lithium fluoride for optical microsystems *Ferroelectric and Dielectric Thin Films (Handbook of Thin Film Materials* vol 3) ed Nalwa H S (San Diego: Academic Press) chap 7, pp 399–431
- [6] Basiev T T, Mirov S B and Osiko V V 1988 *IEEE J. Quantum Electron.* **24** 1052–1069
- [7] Nahum J and Wiegand D A 1967 *Phys. Rev.* **154** 817–830
- [8] Cowley J M 1995 *Diffraction Physics* 3rd ed (Amsterdam: North Holland)
- [9] Pogany A, Gao D and Wilkins S W 1997 *Rev. Sci. Instrum.* **68** 2774–2782
- [10] Lagomarsino S and Cedola A 2004 X-ray microscopy and nanodiffraction *Encyclopedia of Nanoscience and Nanotechnology* vol 10 ed Nalwa H S (USA: American Scientific Publishers) pp 681–710
- [11] Baldacchini G, Bonfigli F, Faenov A, Flora F, Montereali R M, Murra D, Nichelatti E and Pikuz T 2002 *Radiat. Eff. Defects Solids* **157** 569–573
- [12] Baldacchini G, Bonfigli F, Faenov A, Flora F, Montereali R, Pace A, Pikuz T and Reale L 2003 *J. Nanosci. Nanotechnol.* **3** 483–486
- [13] Baldacchini G, Bollanti S, Bonfigli F, Flora F, Di Lazzaro P, Lai A, Marolo T, Montereali R M, Murra D, Faenov A, Pikuz T, Nichelatti E, Tomassetti G, Reale A, Reale L, Ritucci A, Limongi T, Palladino L, Francucci M, Martellucci S and Petrocelli G 2005 *Rev. Sci. Instrum.* **76** 113104–1–12
- [14] Almaviva S, Bonfigli F, Franzini I, Lai A, Montereali R M, Pelliccia D, Cedola A and Lagomarsino S 2006 *Appl. Phys. Lett.* **89** 054102–1–3
- [15] Bonfigli F, Cecilia A, Heidari Bateni S, Nichelatti E, Pelliccia D, Somma F, Vagovic P, Vincenti M A, Baumbach T and Montereali R M 2013 *Radiat. Meas.* **56** 277–280
- [16] URL http://henke.lbl.gov/optical_constants
- [17] Platt U and Stutz J 2008 *Differential Optical Absorption Spectroscopy, Physics of Earth and Space Environments* (Berlin Heidelberg: Springer-Verlag)

- [18] Stabin M G 2008 *Fundamentals of Nuclear Medicine Dosimetry* (Springer Science & Business Media)
- [19] URL <http://www.anka.kit.edu/990.php>
- [20] Durand P, Farge Y and Lambert M 1969 *J. Phys. Chem. Solids* **30** 1353–1374
- [21] Agulló-López F and Jaque F 1973 *J. Phys. Chem. Solids* **34** 1949–1960
- [22] Farge Y 1973 *J. Phys. Colloques* **34 (C9)** C9–475–482
- [23] Soshea R W, Dekker A J and Sturtz J P 1958 *J. Phys. Chem. Solids* **5** 23–33
- [24] Vincenti M A, Montereali R M, Messina G, Nichelatti E, Mancini A and Rufoloni A 2013 Growth and characterisation of thermally-evaporated lithium fluoride thin films for high-energy radiation detectors Tech. rep. ENEA RT/2013/22/ENEA
- [25] Cloetens P, Barrett R, Baruchel J, Guigay J and Schlenker M 1996 *J. Phys. D Appl. Phys.* **29** 133–146
- [26] Mickelson A R 1992 *Physical Optics* (New York: Van Nostrand Reinhold)
- [27] Nichelatti E and Pozzi G 1998 *Appl. Opt.* **37** 9–21
- [28] Goodman J W 1968 *Introduction to Fourier Optics* McGraw-Hill Physical and Quantum Electronics Series (New York: McGraw-Hill Book Company)
- [29] Gaskill J D 1978 *Linear Systems, Fourier Transforms, and Optics* (New York: John Wiley & Sons)
- [30] MathWorks® MATLAB 2010 v. 7.10.0 (r2010a) URL <http://www.mathworks.com>
- [31] Born M and Wolf E 1987 *Principles of Optics* 6th ed (Oxford: Pergamon Press)
- [32] Goodman J W 1985 *Statistical Optics* (John Wiley & Sons)
- [33] De Caro L, Scattarella F, Tangaro S, Pelliccia D, Giannini C, Bottigli U and Bellotti R 2011 *Med. Phys.* **38** 1951–1961
- [34] Baldacchini G, Cremona M, d'Auria G, Martelli S, Montereali R M, Montecchi M, Burattini E, Grilli A and Raco A 1996 *Nucl. Instr. Meth. B* **116** 447–451

Edito dall'ENEA
Servizio Promozione e Comunicazione
Lungotevere Thaon di Revel, 76 - 00196 Roma

www.enea.it

Pervenuto il 17.3.2016

Stampato presso il Laboratorio Tecnografico ENEA - C.R. Frascati
Finito di stampare nel mese di marzo 2016